Journal of Materials Chemistry A

Accepted Manuscript

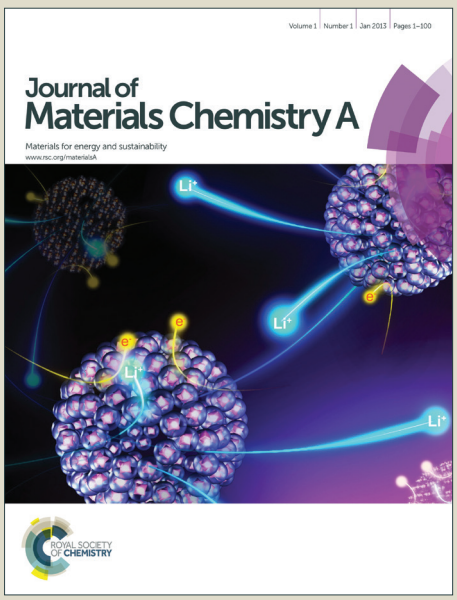

ROYAL SOCIETY OF CHEMISTRY

www.rsc.org/materialsA

Thermally-Enhanced Minority Carrier Collection in Hematite During Photoelectrochemical Water and Sulfite Oxidation

Xiaofei Ye,[a] Jing Yang,[b] Madhur Boloor,[a] Nicholas A. Melosh[a] and William C. Chueh*[a]

[a]Department of Materials Science and Engineering, Stanford University, Stanford, CA 94305, USA.

[b]School of Physics, Peking University, Beijing, 100871, China

Email: wchueh@stanford.edu

Abstract

Many metal-oxide light absorbing semiconductors, such as α-Fe_2O_3 (hematite), exhibit localized small polaron carrier conduction. The low electron/hole mobility hinders minority carrier transport, and is not readily modified through doping or nanostructuring. In this work, we demonstrate that thermal energy, which is available in moderately concentrated sunlight, enhances the minority carrier mobility and photoelectrochemical (PEC) water and sulfite oxidation of 30-nm-thick Ti-doped hematite thin-film photoanodes. In NaOH aqueous electrolyte, the instantaneous Tafel slope at 3 mA cm^{-2} decreases remarkably from 480 mV dec^{-1} (at 7 ^{o}C) to 240 mV dec^{-1} (at 72 ^{o}C) under 9 suns illumination, representing a substantial increase in the fill factor, which also depends on the doping level. Though the photovoltage decreases with temperature expectedly, we show that it can be mitigated by increasing the light intensity. In presence of a Na_2SO_3 hole scavenger, the photocurrent at 1.23 V *vs* reversible hydrogen electrode increased from 3.1 (at 7 ^{o}C) to 5.0 mA cm^{-2} (at 72 ^{o}C) under 8 suns illumination, and the onset potential was shown to be weakly dependent on the temperature. The strong increase in the photocurrent with temperature in the limit of fast reaction kinetics suggests that it arises from an improvement in the collection of minority carriers in the diffusion region of hematite. We show that room temperature and 1 sun illumination intensity is not the optimal reaction operating condition for hematite photoanodes. The

thermally-enhanced minority carrier transport are likely generalizable to other small-polaron-type light absorbers for PEC and solar cells.

Introduction

Photoelectrochemical (PEC) cells have been explored extensively for light-driven dissociation of water to hydrogen and oxygen.[1] Presently, an overwhelming majority of the research is focused on PEC cells operating at room temperature, largely due to the decreasing photovoltage[2, 3] and limited electrolyte stability with increasing temperatures.[4] The former arises from increased intrinsic carrier concentration and reverse saturation current with temperature, as observed widely in photovoltaic cells.[2, 3] Despite these drawbacks, however, thermal energy improves many aspects of photoelectrochemistry, such as carrier transport and electrocatalysis. Recent efforts to understand temperature effects have largely focused on the electrocatalysis rate and the reverse saturation current. Temperature effects on charge transport and minority carrier diffusion remain largely unexplored.[5-7]

It is increasingly recognized that many metal-oxide photoelectrodes exhibit a small-polaron-type conduction mechanism, and that the carrier mobility increase significantly with temperature. Examples include Fe_2O_3,[8, 9] $BiVO_4$,[10] and $(La,Sr)FeO_{3-\delta}$.[11] The thermally-activated nature of small-polaron transport offers a path towards improving the minority carrier mobility, which is not readily attained by doping or nanostructuring. Moreover, in addition to reducing the thermodynamic potential for water splitting (approximately -0.8 mV K^{-1} below 100 ^oC, and -0.2 mV K^{-1} above 100 ^oC), thermal energy also enhances the rate constants of the electrocatalytic reactions (activation energies typically ranging from 0.1 to 1 eV).[12-16] Numerous on-cell schemes for increasing temperature and optical concentrations have been investigated.[17-20] Utilizing thermal energy in PECs could make stable and abundant materials, otherwise inadequate at ambient temperature, viable.

For particulate photocatalyts such as TiO_2, there have been a few experimental demonstrations of appreciable solar-to-hydrogen efficiency improvement with temperature.[21-23] Several device-level implementations using concentrated sunlight were proposed.[24-27] Temperature effects in

photoelectrochemical solar cells have also been explored for semiconductor/redox electrolyte system, where in most cases, increasing temperature leads to an improvement in the efficiency,[28-32] though it typically peaks at temperature slightly above ambient. In these light absorbers, carrier conduction takes place via delocalized bands, and the mobility generally decreases weakly with temperature. Therefore, the observed enhancement likely arose from enhanced electrocatalytic reaction rates, rather than from improved charge transport and minority carrier diffusion.

Hematite, the most oxidized form of iron oxide and a small-polaron semiconductor, is a promising photoanode due to its high natural abundance, suitable band-gap for water splitting, and excellent stability in aqueous environment.[33, 34] However, there are three major issues that limit the solar-to-fuel efficiency of hematite-based photoanodes: (1) the low mobility[35] and the short lifetime of minority carriers,[36, 37] (2) the low catalytic activity for oxygen-evolution reaction (OER)[38] and (3) the high surface recombination rate.[39] Substantial efforts are underway to overcome these challenges, including the use of nanostructures[40-42] and ultra-thin films[43, 44] for efficient charge separation, surface modification by electrocatalysts such as IrO_2,[42] cobalt phosphate (Co-Pi)[45] and $NiFeO_x$[46] to improve the catalytic activity, and surface passivation by Al_2O_3 and Ga_2O_3 to lower the surface carrier recombination rate.[47-49] Despite improving the photoactivity considerably, these approaches do not address the crucial material limitation in hematite: the low carrier mobility, much less than *ca.* 0.1 $cm^2\ V^{-1}\ s^{-1}$ at room temperature, and thus short minority carrier diffusion length ($L_D=\sqrt{D\tau}$, where L_D is diffusion length, D is diffusivity and τ is carrier lifetime).[9, 50, 51] Experimentally-measured electron and hole mobilities of hematite show a thermal activation with an activation energy of 0.1 to 0.6 eV (depending on the doping level), typical of small-polaron conduction.[9, 35, 50-53] The carrier lifetime inside the space-charge region has also been measured in-situ using transient absorption spectroscopy in the presence of a hole scavenger, and was found to depend very weakly on temperature. Moreover, Cowan *et al.* also observed a significant activation barrier (*ca.* 0.5 eV) for hole transfer at the α-Fe_2O_3/electrolyte interface.[54] These observations suggest that thermal energy can be a crucial factor for enhancing hematite-based photoanodes.

In this work, we systematically investigate the effects of temperature and light intensity on the photoelectrochemical properties of dense Ti-doped hematite thin-film electrodes grown by pulsed-laser deposition (PLD) for water and sulfite oxidation. We observe a significant enhancement in the photocurrent under heating and concentrated illumination. Specifically, the increase in the small-polaron-type minority carrier mobility with temperature leads to an enhancement in the collection of minority carriers. For water oxidation, the instantaneous Tafel slope increases substantially with temperature, giving a higher fill factor. For sulfite oxidation, which exhibits fast interfacial kinetics, both the Tafel slope and the photocurrent increase substantially with temperature. These results are likely generalizable to other small-polaron-type light absorbers.

Experimental Section

Sample preparation

Ti-doped α-Fe_2O_3 thin films were deposited by PLD (PLD/MBE-2300, PVD Products). The ablation targets were fabricated by solid-state reaction method. Fe_2O_3 powder (99.999%, Alfa Aesar) was mixed with TiO_2 powder (0.1 at.%, 1 at.% or 5 at.%, 99.99% purity, Sigma-Aldrich), pressed uniaxially at 60 MPa and then sintered in 21% O_2 balanced with Ar at 1250 ^{o}C for 10 hours. Two types of substrates were used. For current-voltage measurements with front-side illumination, the films were grown on platinized sapphire (0001) substrates. The bare sapphire substrates (MTI Corp.) were first sonicated in isopropanol for 10 minutes and then coated with 200 nm platinum via radio-frequency magnetron sputtering (200 W) from a platinum sputter target (99.99% Alfa Aesar) in 5 mTorr Ar. Additional samples for open-circuit potential (OCP) measurements with backside illumination were grown on fluorine-doped SnO_2 coated glass substrates (MTI Corp.). The α-Fe_2O_3 thin film was deposited by PLD using a KrF (248 nm) excimer laser at a fluence of 1 J cm^{-2} and a repetition rate of 4 Hz. The depositions were performed at a temperature of 450 ^{o}C (infrared heater) and in 10 mTorr O_2. The substrate to target distance was kept at 100 mm.

Photoelectrochemical characterization

Photoelectrochemical characterization was carried out in a temperature-controlled, single-compartment Teflon cell. The electrolyte was 0.1 M NaOH aqueous solution (Fisher Scientific) for water oxidation, and 1 M Na_2SO_3 and 0.6 M NaOH (Sigma-Aldrich) aqueous solution for sulfite oxidation. The electrolyte for OCP measurement was 1 mM $K_3Fe(CN)_6$, 100 mM $K_4Fe(CN)_6$, and 1 M NaOH (Sigma-Aldrich) aqueous solution. The Teflon cell was immersed in a water bath connected to a thermostatic circulator. The temperature of the electrolyte, measured via a PFA coated T-type thermocouple, was varied between 7 and 72 ^{o}C. The typical temperature variation for a given set point was ± 0.5 ^{o}C. A platinum wire (Sigma Aldrich) was used as the counter electrode, and a reversible hydrogen electrode (RHE) (eDAQ Inc.) was used as the reference electrode. The variation in pH value due to water evaporation during the experiment was within 0.1. We note that the hydrogen electrode directly sensed the RHE potential in the electrolyte at a given temperature. The sample was mounted and sealed onto the Teflon cell with a silicone O-ring encapsulated in fluorinated ethylene propylene. During the photoelectrochemical measurement, the sample was illuminated by a solar simulator (350-1100 nm, HAL-320, Asahi Spectra Inc.), the spectrum of which was verified by a UV-visible spectrometer (USB2000+, Ocean Optics). The illumination area is 0.255 cm^2. The illumination flux was calibrated by a thermopile sensor (Scientech Inc.) to attain 79 mW cm^{-2} (1 sun) within the wavelength range of 350-1100 nm. Higher fluxes were obtained by adjusting the focusing optics. Thermocouple placed close to the sample confirmed that the sample temperature did not change appreciably with illumination during typical measurement intervals. The electrolyte was purged by nitrogen for one hour before the measurements. During the measurement, the nitrogen flowed overhead the electrolyte continuously. The three-electrode cyclic voltammetry were measured by a Bio-Logic SP-240 potentiostat. The series resistence was subtracted which was determined by electrochemical impedance spectroscopy.

Results and Discussion

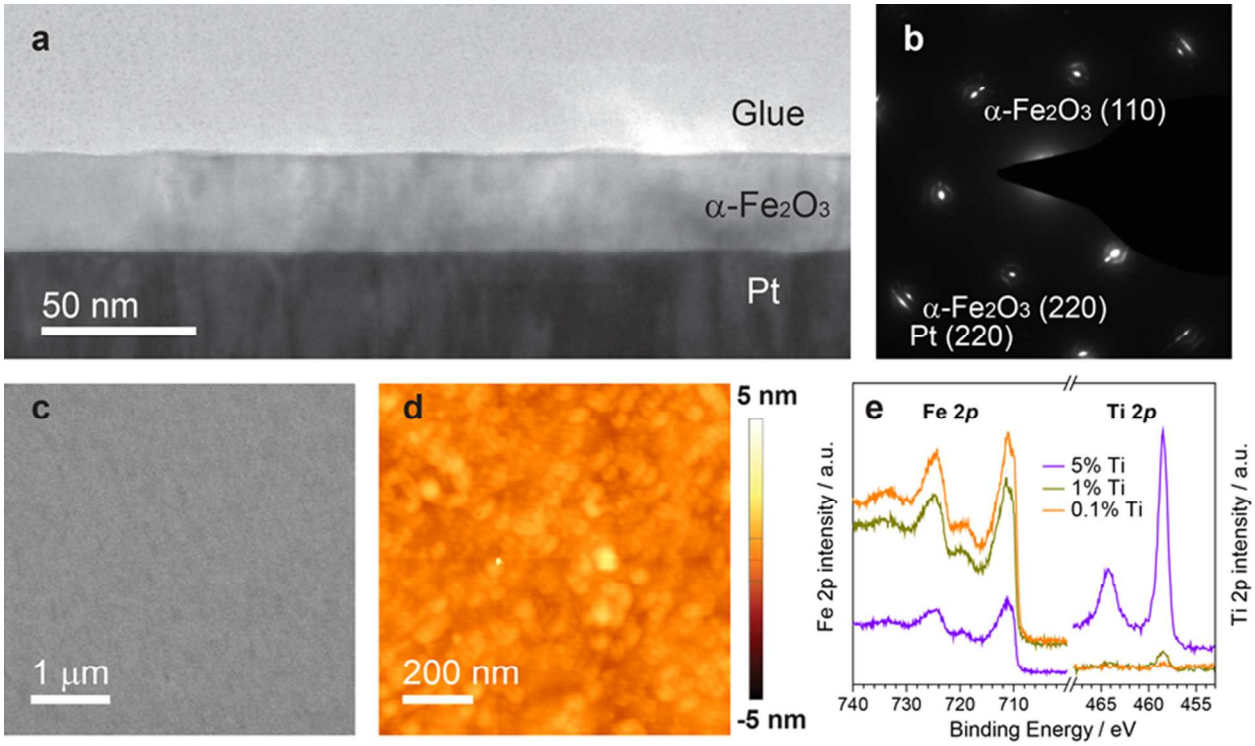

Fig. 1 (a) Cross-sectional TEM image, (b) selected area electron diffraction, (c) SEM image, and (d) AFM image for 5% Ti-doped α-Fe_2O_3 thin film on a platinized sapphire substrate. (e) Fe 2*p* and Ti 2*p* core level XPS for α-Fe_2O_3 thin films as a function of dopant concentrations.

The PLD growth produced high-quality α-Fe_2O_3 thin films on platinized sapphire substrates. The thickness of the film was chosen to be ~30 nm (and verified by cross-sectional transmission electron microscopy (TEM) (Fig. 1a)), in order to attain sufficient light absorption which is not limited by the width of the space charge region and majority carrier transport.[43, 44] The crystal phase was verified to be hematite by selected area diffraction (Fig. 1b). The surface morphology of the α-Fe_2O_3 thin films on platinized sapphire substrates was characterized by scanning electron microscopy (SEM) and atomic force microscopy (AFM) (Fig. 1c and d). Consistent with previous reports of hematite grown by PLD, the films are dense and flat with a root-mean-square roughness below 1 nm. Finally, the X-ray photoelectron spectroscopy (XPS) shows that the measured Ti concentration is consistent with the nominal doping level (Fig. 1e).

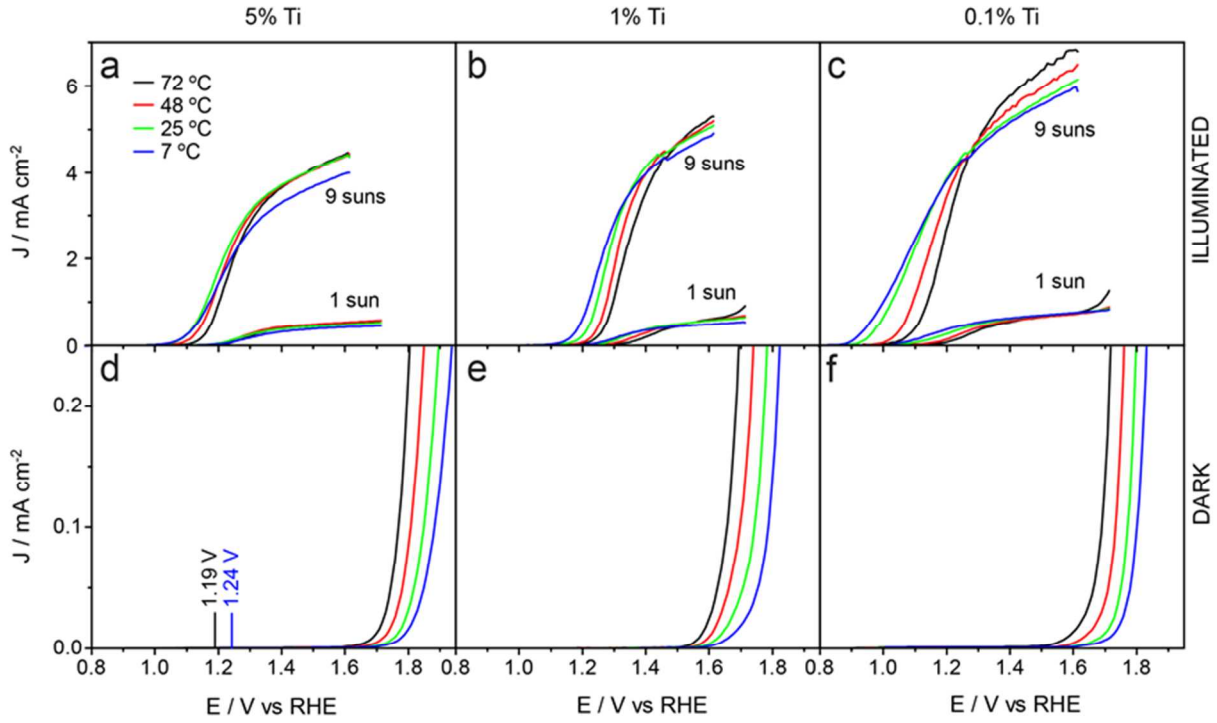

Fig. 2 Temperature-dependent current-voltage curves of hematite photoanodes doped with nominally 5% (a, d), 1% (b, e), and 0.1% (c, f) Ti, under illumination (a, b, c) and in the dark (d, e, f). The thermodynamic redox potentials for OER at 72 °C and 7 °C are shown in (d).

Current-voltage curves for 5%, 1%, and 0.1% Ti-doped α-Fe_2O_3 thin film photoanodes were measured between 7 and 72 °C and light intensity between 1 and 9 suns. Fig. 2a-c shows the photocurrent densities, while Fig. 2d-f shows the corresponding dark current densities. Additionally, we also examined the stability of the photoelectrode under constant current conditions at 70 °C and 9 suns light intensity (Fig. 3). Beyond periodic changes in potential due to the formation of bubbles and possible drift in temperature, no appreciable degradation was observed over 4.5 hours. We first analyze the electrochemical behavior in the dark: the current densities show a consistent cathodic shift with increasing temperature, regardless of doping level. In hematite, the poor diode characteristic of the hematite/electrolyte interface leads to significant current leakage, and that the dark current is limited by the rate of electrocatalysis. This is confirmed by the low onset potential in the dark when a fast redox couple is used (Fig. S1 in ESI). From 7 to 72 °C, the cathodic shift in the dark, *ca.* 110 to 140 mV, is significantly greater than the thermodynamic shift in equilibrium redox potential of the OER (*vs* RHE),

50 mV. This observation indicates a thermally-activated barrier that limits the rate of OER at the α-Fe_2O_3/electrolyte interface. This can be seen more explicitly in the Tafel plot where we observe a 60 to 90 mV decrease in overpotential when the temperature is increased from 7 ^oC to 72 ^oC (Fig. S2 in ESI). In addition, the Tafel slope in the dark shows a weak dependence on temperature and dopant concentration in the photoelectrodes examined (see ESI for more details).

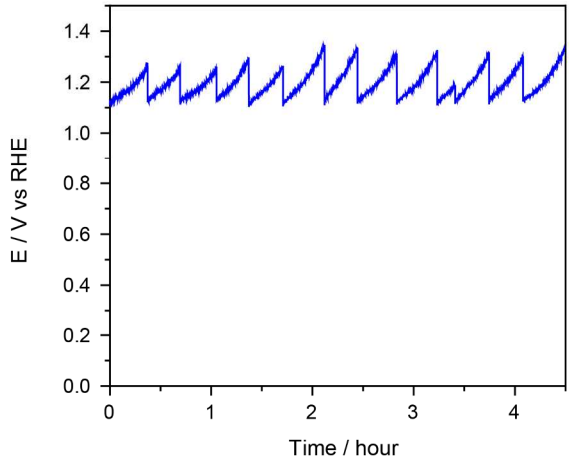

Fig. 3 Chronopotentiometry of a 0.1% Ti-doped α-Fe_2O_3 photoanode over 4.5 hours in 0.1 M NaOH aqueous solution at 70 ^oC and under 9 suns illumination. The current was held at 2 mA cm^{-2}. The light was turned off every 20 minuntes to clear off the bubbles and stabilize the possible temperature drift.

Under 1 sun illumination at 25 ^oC, the photocurrent density of the dense 0.1% Ti-doped film is 0.33 and 0.76 mA cm^{-2} at 1.23 V and 1.60 V *vs* RHE, respectively, which is comparable to the activity of bare hematite thin film photoanodes reported in literature.[44, 55] As we increase the illumination intensity, the photocurrent densities show a considerable cathodic shift, indicating a larger Fermi level splitting within the hematite thin films due to a higher electron/hole pair generation rate under concentrated light illumination. As shown in Fig. 4, the onset potential, determined at a current density of 5.9×10^{-3} mA cm^{-2}, scales logarithmically with light intensity, approximately 120 mV per decade. This scaling is greater than that observed by Wang et al,[56] indicating a more efficient separation of electron/hole pairs in our electrodes, especially under high generation rates. The onset potentials do not exhibit a monotonic

dependence on dopant concentration due to a mixed effect of dopant concentration on electrocatalytic activity, photovoltage, light absorption, etc.

Turning to the temperature dependence under illumination, the onset potential of the photocurrents shifts anodically with increasing temperatures and decreasing doping level. This contrasts with the behavior of the dark current. We separated the temperature dependence of the onset potential into two contributions: the shift in the equilibrium redox potential, and the change in the photovoltage. Here, the photovoltage is defined phenomenologically as the difference between the onset potential under illumination and the OER redox potential.[57] The OCP, measured in a well-defined redox-couple, is presented later. Fig. 5 shows the deconvolution, taking the onset potential measured at 25 ^{o}C and 1 sun as a baseline. For the 5% Ti-doped electrode, increasing temperature at 1 sun from 25 to 72 ^{o}C decreases the equilibrium redox potential by 40 mV, but decreases the photovoltage by 74 mV. We also observed that the temperature dependence of the photovoltage weakens with increasing dopant concentration (Fig. 5). This observation is consistent with the fact that the electrons generated by doping dominate over thermally generated electrons, *i.e.*, the material becomes less intrinsic at higher doping levels. While increasing the temperature lowers the photovoltage, it also lowers the redox potential for the OER. The decrease in photovoltage is due to a rise in the reverse saturation current as observed in photovoltaic cells.[2, 3] Higher optical concentration, on the other hand, increases the photovoltage. Combined, heating and optical concentration lower the onset potential for 5% and 1% Ti-doped electrodes. This finding is particularly advantageous to PEC systems since an increase in cell temperature accompanies optical concentration, unless the cell is cooled.

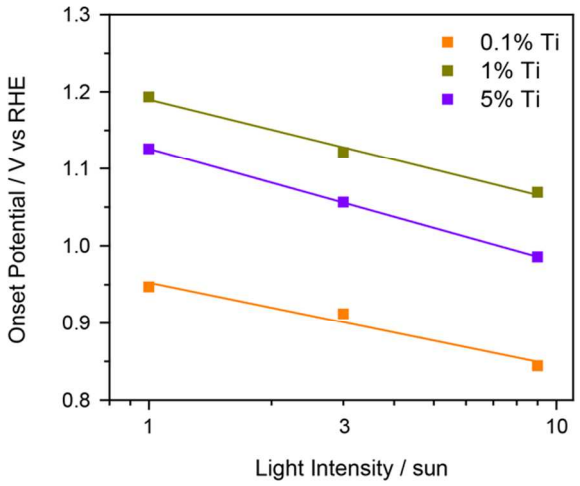

Fig. 4 Onset potential at 25 °C as a function of the illuminated light intensity. Onset potential is defined as the potential at a current density of 5.9×10^{-3} mA cm^{-2}. Lines are apparent linear fits to the data.

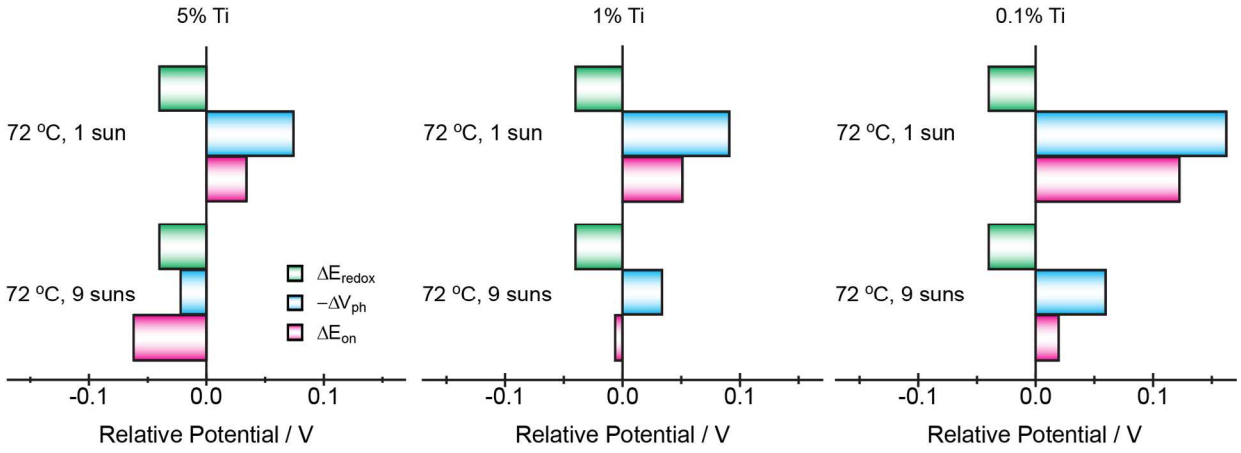

Fig. 5 Contributions to the potential (*vs* RHE) difference under different conditions for 5%, 1% and 0.1% Ti-doped samples. E_{redox} represents the thermodynamic OER potential. V_{ph} and E_{on} represent photovoltage and onset potential under illumination, respectively. See text for definitions. Taken relative to potentials at 25 °C and 1 sun.

Another noticeable feature in Fig. 2 is the dependence of the curvature of the photocurrent-voltage traces on temperature. To compare the photocurrent under different illumination intensity, we examined the photocurrent density normalized by the incident light intensity (Fig. 6a). This quantity gives the photoelectrode area needed to achieve a given hydrogen/oxygen generation rate, and is useful for

comparing between different operating conditions. Under most potentials, the normalized photocurrent under 9 suns illumination exceeds that under 1 sun. We note that the photocurrent does not necessarily scale linearly with the light intensity. In hematite, it has been observed that the photocurrent exhibits a sub-linear dependence on light intensity due to the increased recombination rate under high generation rate conditions.[58]. Therefore, our observation here indicates efficient electron/hole separation. Fig. 6b shows the amount of the cathodic shift at 0.3 mA cm^{-2} sun^{-1} for all doping levels and temperatures at 9 suns, again relative to the baseline case at 25 °C and 1 sun. With increasing temperature, the extent of cathodic shift decreases. At 48 °C, this cathodic shift is between 25 and 37 mV.

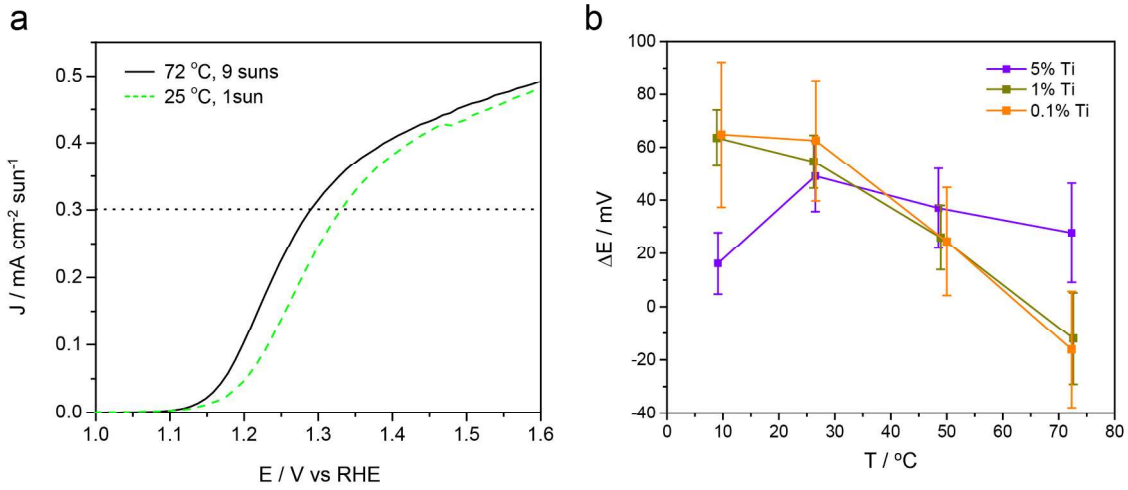

Fig. 6 (a) Current-voltage curves normalized by the light intensity for 5% Ti-doped sample under 9 suns illumination at 72 °C (black), and under 1 sun and 25 °C (green). (b) Applied potentials to attain 0.3 mA cm^{-2} sun^{-1} under 9 suns illumination at various temperatures. Taken relative to the applied potential under 1 sun illumination at 25 °C. Error bars are calculated based on one standard deviation of multiple runs.

Next, we discuss the instantaneous Tafel slope of current-voltage curves, which is revealed in a semi-log Tafel plot (Fig. 7). The Tafel slope under illumination below ~0.4 mA cm^{-2} is essentially the same as in the dark, and is furthermore independent of temperature. This observation indicates that the photocurrent in this regime is limited by the same mechanism as the dark current, consistent with our observation that slow reaction kinetics limits the α-Fe_2O_3/electrolyte interface (Fig. S1 in ESI).[38] As the

photocurrent increases, however, the Tafel slope decreases significantly faster as the temperature is increased. In other words, at higher temperatures, the photocurrent shows a sharp transition from a reaction-limited regime to a saturated regime, while at low temperatures, the transition is considerably more gradual. Such a fast transition at elevated temperature is analogous to a large fill factor in a solar cell.[59] The temperature dependence here contrasts with that of photovoltaic cells, in which the fill factor decreases with temperature.[60, 61] Above a photocurrent of ~4 mA cm^{-2}, the photocurrent saturates and the Tafel slope approaches infinity. In this saturated regime, we note that the saturation current depends weakly on temperature because the charge separation in hematite at large potentials for water oxidation takes place primarily in the space-charge region, the width of which does not depend strongly on temperature.

We evaluated the potential change needed to increase the photocurrent from 8% to 80% of the saturation current density at 1.6 V *vs* RHE (Fig. 8), *i.e.*, the average Tafel slope. The temperature dependence of such potential change is most pronounced in the 0.1% Ti-doped sample, decreasing from 393 (at 7 ^{o}C) to 198 mV (at 72 ^{o}C) under 9 suns illumination, and less so for the other doping levels. We rationalize the dependence of the Tafel slope on the doping level as follows: as doping level increases, the majority carrier concentration becomes increasingly pinned (*i.e.*, extrinsic) under illumination, and thus quasi-Fermi level splitting is less sensitive to temperature. Alternatively, it is also possible that the lower doping level gives rise to a lower recombination rate.

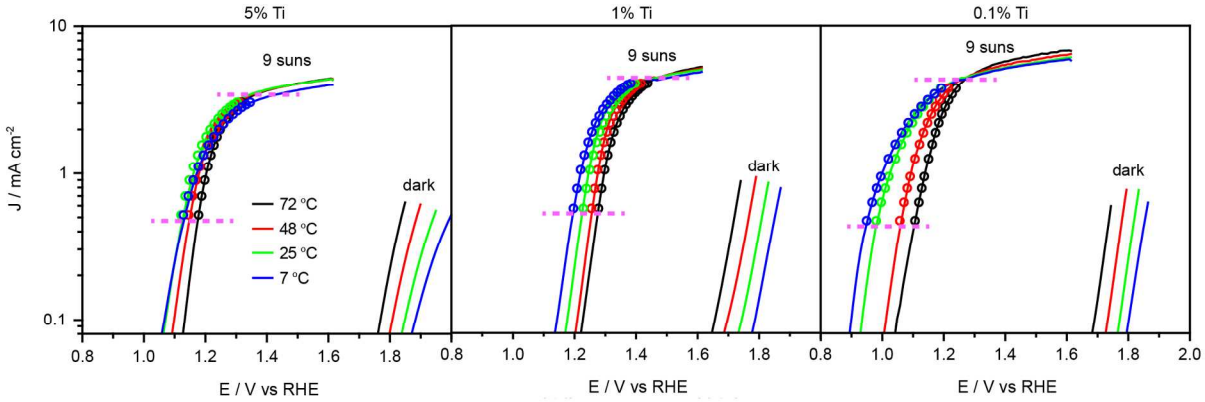

Fig. 7 Semi-log plot of the current-voltage curves in the dark and under 9 suns illumination for the 5%, 1% and 0.1% Ti-doped hematite photoanode at various temperatures. Dashed lines indicate the transition regime. The circle markers represent the fitting in the transition regime.

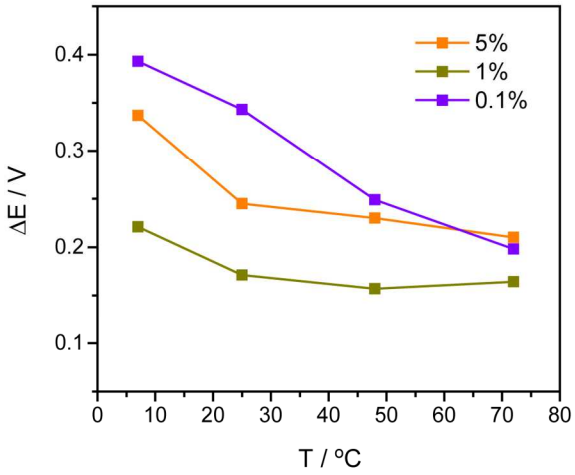

Fig. 8 Potential change needed to increase the photocurrent from 8% to 80% of the saturation current density at 1.6 V *vs* RHE at various temperatures.

In order to understand the beneficial temperature effect on the Tafel slope (*i.e.*, fill factor) under illumination, we consider the hematite photoanode as a Schottky junction solar cell, with its current collection interface shared with an electrolyzer, and we obtain the following relationship of the Tafel slope:

$$\frac{\partial V_{bias}(j)}{\partial j} \approx \frac{\partial \eta(j)}{\partial j} + \frac{k_B T}{q} \frac{n_{id}}{j_{SC}} \quad (1)$$

where V_{bias} is the bias, j_{SC} is the short circuit current, and q, k_B, and T have their usual meanings. The diode ideality factor n_{id} can be regarded qualitatively as a measure of recombination and charge transfer properties of the hematite/electrolyte junction (see ESI for derivation). Experimentally, we observe that the overpotential $\eta(j)$ scales logarithmically with the current density and is independent of temperature. At low photocurrent density, the final term in Equation (1) is negligible. As a result, the Tafel slope under illumination tracks that of the dark. This represents the reaction-limited region, as already discussed. As the photocurrent rises, the final term becomes increasingly dominant and V_{bias} scales linearly with the current density. In an equivalent circuit sense, the final term can be viewed as a resistor in series with the light absorber. We fit the photocurrent in the transition region to Equation (1). The fit, shown as open markers in Fig. 7, is excellent. The fitting parameter, j_{SC}/n_{id}, is shown in the Arrhenius plots (Fig. 9) and the activation energies are summarized in Table 1.

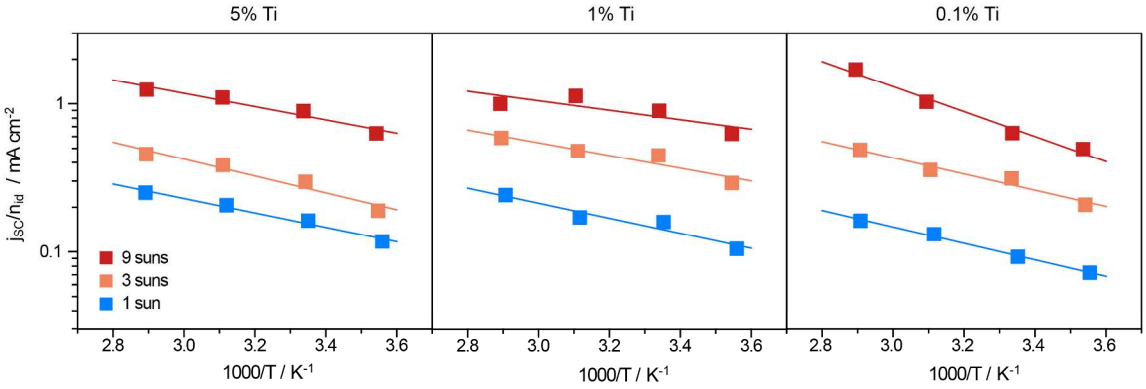

Fig. 9 Arrhenius plot (markers) and fit (lines) of the extracted j_{SC}/n_{id} for 5%, 1% and 0.1% Ti-doped α-Fe_2O_3. Activation energies shown in Table 1.

Table 1. Apparent activation energy of j_{SC}/n_{id}.

Light Concentration [sun]	Activation Energy [eV]		
	5% Ti-doped	1% Ti-doped	0.1% Ti-doped
1	0.10 ± 0.01	0.10 ± 0.02	0.110 ± 0.005
3	0.11 ± 0.02	0.09 ± 0.02	0.11 ± 0.02
9	0.09 ± 0.01	0.06 ± 0.03	0.17 ± 0.02

As can be seen, j_{SC}/n_{id} is thermally activated with the apparent activation energies between 0.06 and 0.17 eV under the illumination intensities examined. On one hand, the thermal enhancement of j_{SC} can be attributed to the increasing effective absorption length at elevated temperature due to the thermally enhanced minority carrier mobility, and thus the minority carrier diffusion length, even though the carrier lifetime likely decreases slightly with temperature.[35] On the other hand, n_{id} reflects the current collection efficiency at the α-Fe_2O_3/electrolyte interface. As the temperature increases, the photo-generated carriers are collected more efficiently at the interface, *i.e.* through the OER, rather than recombine via the interfacial trap states. In short, the combined effect of the reduced ideality factor n_{id} and the enhanced short circuit current j_{SC} results in a smaller series resistance and thus smaller Tafel slope at elevated temperatures. Here, we recognize the temperature dependence of the interfacial reaction kinetics complicates the analysis.

In order to deconvolute the temperature effect on the reaction kinetics and minority carrier diffusion, we also investigated the temperature dependent current-voltage characteristic in an aqueous electrolyte with a hole scavenger (1M Na_2SO_3 and 0.6M NaOH) (Fig. 10). In the presence of a hole scavenger, the interfacial reaction kinetics is considered sufficiently fast such that all photo-generated holes reaching the hematite/electrolyte interface are collected effectively. Even in the absence of quantitative analysis, the PEC activity for sulfite oxidation is strongly activated by temperature. Because majority carrier transport resistance is negligible in the thin-film electrode geometry, we expect the temperature dependence to arise primarily from minority carrier diffusion. Analysis of the current-voltage curves reveals that the onset potential for sulfite oxidation does not depend strongly on temperature (Fig. 11a), which contrasts with that for water oxidation. Moreover, the temperature dependence of the photocurrent is more prominent with the hole scavenger than without. In particular, raising the temperature from 7 ^{o}C to 72 ^{o}C increases the photocurrent at 1.23 V *vs* RHE by 40% for 5% Ti-doped hematite, and similarly for the other doping levels (Fig. 11b). The decrease in the instantaneous Tafel slope at ~ 1 V *vs* RHE confirms that the enhancement of the minority carrier diffusion with temperature overwhelms the decrease in the photovoltage and increase in recombination. The observations here

provide further evidence that carrier mobility rather than lifetime dominates the temperature dependence of the minority carrier diffusion length. The fact that such a thermal enhancement is more prominent in the electrolyte with hole scavenger than without reflects the key role of the reaction kinetics. Without co-catalysts and hole scavengers, the photo-generated carriers are prone to recombine at the hematite/electrolyte interface due to the slow reaction kinetics, and mask the beneficial role of thermal energy.

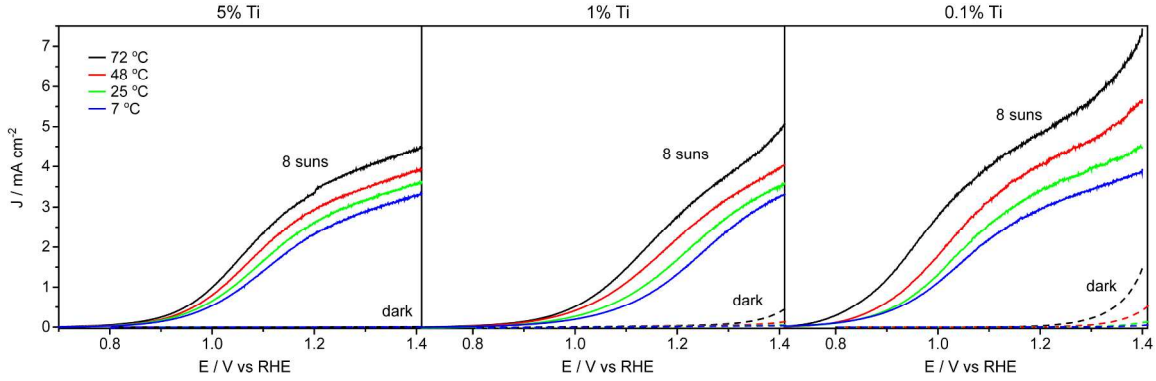

Fig. 10 Temperature-dependent current-voltage curves of hematite photoanodes in hole scavenger solution for 5%, 1% and 0.1% Ti doping.

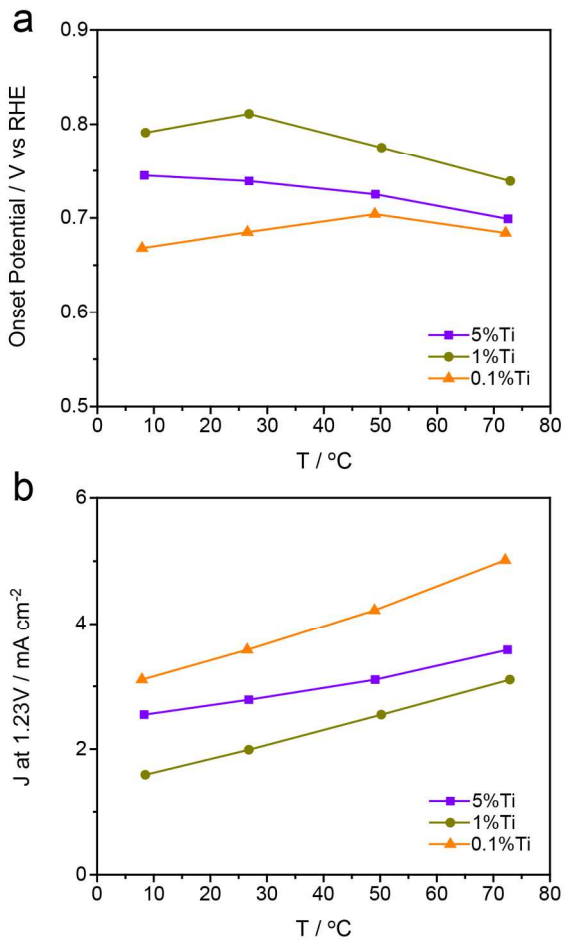

Fig. 11 (a) Onset potential at 0.01 mA cm^{-2} and (b) photocurrent at 1.23 V *vs* RHE as a function of temperature under 8 suns in hole scavenger solution.

In addition to quantifying the photocurrent, onset potential, and the instantaneous Tafel slope under illumination, we also examined the temperature dependence of the photovoltage. In order to obtain a well-defined photovoltage, we employed a ferri/ferrocyanide reversible redox couple.[62, 63] Specifically, we used 1 mM $K_3Fe(CN)_6$ and 100 mM $K_4Fe(CN)_6$ in 1 M NaOH aqueous solution which gives an equilibrium redox potential at 1.17 V *vs* RHE. The close proximity to the OER redox potential gives a similar degree of band bending at the hematite/electrolyte interface. Moreover, the low concentration of electron acceptor ($K_3Fe(CN)_6$) minimizes the electron transfer between the redox couple and hematite. In general, the change in OCP under illumination versus in the dark does not necessarily represent

photovoltage or quasi Fermi level splitting in the semiconductor unless a reversible redox couple is used because the hole quasi Fermi level is not likely aligned with the OER level due to its slow charge transfer kinetics.

Since ferri/ferrocyanide solution is yellowish in color, we used back illumination cell geometry with a α-Fe_2O_3 thin film grown on fluorine-doped tin oxide coated glass substrate (see Experimental Section for details). Due to possible tin diffusion into the thin-film electrode during growth,[41] a highly doped (5% Ti) α-Fe_2O_3 was examined so that the film remains intentionally doped. In the dark, both the hematite working electrode (WE) and the Pt counter electrode (CE) exhibit the same potential due to the fast reaction kinetics of the ferri/ferrocyanide redox couple on both electrodes (Fig. 12a). Under illumination, the CE remains aligned with the reversible redox level, while in the hematite WE, the quasi Fermi level splitting causes the hole quasi Fermi level to align with the redox couple, again due to the fast kinetics of the reversible redox couple (Fig. 12b). Thus, the OCP difference between the two electrodes represents the photovoltage or the quasi Fermi level splitting in the hematite. Fig. 12c shows the OCP in the dark and under illumination. The potential of the Pt CE is stable throughout the measurement and is taken as the ferri/ferrocyanide redox potential. This ferri/ferrocyanide redox potential decreases with increasing temperature for about 0.1 V (*vs* RHE) within the investigated temperature range, which is consistent with its reported thermodynamic value.[64] Fig. 12d plots the photovoltage as a function of temperature under 1 sun and 3 suns illumination. The photovoltage deceases with temperature and increases with light intensity, consistent with the behavior of the photovoltage shown in Fig. 5.

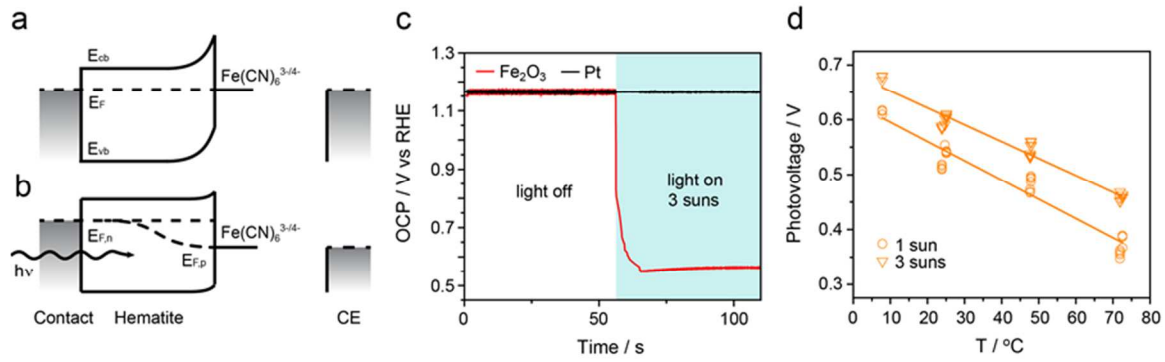

Fig. 12 Schematic energy band diagram for hematite photoanode in contact with ferri/ferrocyanide redox couple in the dark (a) and under illumination (b). (c) OCP measurement with light on and off under 3 suns illumination and 25 °C. (d) Temperature dependence of the photovoltage under 1 and 3 suns. Lines are linear fits to the data. Shown for the 5% Ti-doped hematite photoanode.

Table 2. Temperature coefficient and activation energy of the photovoltage.

	α/q [mV K^{-1}]	E_a [eV]
1 sun	-3.6 ± 0.2	1.59 ± 0.05
3 suns	-3.1 ± 0.1	1.52 ± 0.04

From the knowledge of solar cell analysis, the temperature dependence of the photovoltage can be modeled phenomenologically as[65]

$$qV_{ph} = E_a + \alpha T \tag{2}$$

where

$$\alpha = -n_{id} k_B \ln \frac{j_{00}}{j_{SC}} \tag{3}$$

and E_a is the activation energy and j_{00} is the pre-exponential factor of the reverse saturation current. Based on Equation 2, we performed a linear fit of the photovoltage as a function of temperature (Fig. 12d). The excellent fit indicates that the temperature coefficient α is essentially constant under the conditions examined, which ranges from -3.1 to -3.6 mV K^{-1}, for 1 and 3 suns illumination, respectively (Table 2). For comparison, the temperature dependence of the open-circuit voltage for single-junction Si and GaAs

solar cells is approximately -2 mV K^{-1}.[61] The activation energy E_a obtained from the linear fit is between 1.5 and 1.6 eV. We note that this value is smaller than 2.1 eV, the α-Fe_2O_3 band-gap at room temperature. If one considers the α-Fe_2O_3/electrolyte junction as similar to a Schottky junction, the reverse saturation current is composed of the minority carrier diffusion current in the bulk (*i.e.*, holes from α-Fe_2O_3 to electrolyte), and the majority carrier emission current at the α-Fe_2O_3/electrolyte interface (*i.e.*, electrons transferred from hydroxyl ions in the electrolyte or from interfacial trap states).[66] We expect that the minority carrier diffusion current to exhibit an activation energy close to the α-Fe_2O_3 band-gap,[61] while the majority carrier emission current to exhibit an activation energy of the interfacial barrier[65] (see ESI for more details). Thus, E_a being smaller than the band-gap indicates that the interfacial recombination dominates over the bulk recombination, at least for the 5% Ti-doped α-Fe_2O_3. Ideally, when α-Fe_2O_3 surface is well passivated, E_a should be close to 2.1 eV.

Conclusion

We have shown that room temperature and 1 sun illumination intensity is not the optimal reaction operating condition for hematite photoanodes, which is likely generalizable to other small-polaron-type light absorbers. Under the combined effect of heating and optical concentration, hematite photoanodes exhibit a lower onset potential and higher photocurrent density. Though the charge carrier lifetime generally decreases slightly with temperature, the greater dependence of the small polaron mobility on temperature improves the minority carrier diffusion length significantly at elevated temperatures. By analyzing the temperature dependence of the photocurrent and the photovoltage, we show that the enhanced minority carrier diffusion length in the bulk and the faster charge transfer kinetics at the α-Fe_2O_3/liquid interface give rise to the improved photoelectrochemical properties at elevated temperatures. This positive temperature effect could open up new approaches of utilizing moderately concentrated sunlight in PEC cells. Conventional concentrated photovoltaic solar cells require active or passive cooling to prevent the device from heating up,[67] thereby lowering the overall system efficiency. Photoelectrodes

under moderately concentrated illumination, however, would benefit from the thermal enhancement and not require the cooling.

Acknowledgements

This work was funded by the Precourt Institute for Energy and the Global Climate and Energy Project at Stanford University. X.Y. was supported by the Stanford Graduate Fellowship. J.Y. was supported by the Chinese Undergraduate Visiting Research Program and M.B. was supported by the National Science Foundation Graduate Research Fellowship under Grant No. DGE-114747.

References

1. M. G. Walter, E. L. Warren, J. R. McKone, S. W. Boettcher, Q. Mi, E. A. Santori and N. S. Lewis, *Chem. Rev.*, 2010, **110**, 6446-6473.
2. S. M. Vernon and W. A. Anderson, *Appl. Phys. Lett.*, 1975, **26**, 707-709.
3. J. J. Wysocki and P. Rappaport, *J. Appl. Phys.*, 1960, **31**, 571-578.
4. S. Bose, T. Kuila, N. Thi Xuan Lien, N. H. Kim, K.-t. Lau and J. H. Lee, *Prog. Polym. Sci.*, 2011, **36**, 813-843.
5. Y. Chen, S. Hu, C. Xiang and N. Lewis, *Energy Environ. Sci.*, 2015, **8**, 876-886.
6. S. Haussener, S. Hu, C. X. Xiang, A. Z. Weber and N. S. Lewis, *Energy Environ. Sci.*, 2013, **6**, 3605-3618.
7. X. F. Ye, J. Melas-Kyriazi, Z. L. A. Feng, N. A. Melosh and W. C. Chueh, *Phys. Chem. Chem. Phys.*, 2013, **15**, 15459-15469.
8. A. J. Bosman and H. J. Vandaal, *Adv. Phys.*, 1970, **19**, 1-117.
9. R. F. G. Gardner, F. Sweett and D. W. Tanner, *J. Phys. Chem. Solids*, 1963, **24**, 1175-1181.
10. A. J. E. Rettie, H. C. Lee, L. G. Marshall, J.-F. Lin, C. Capan, J. Lindemuth, J. S. McCloy, J. Zhou, A. J. Bard and C. B. Mullins, *J. Am. Chem. Soc.*, 2013, **135**, 11389-11396.
11. E. V. Tsipis, M. V. Patrakeev, V. Kharton, A. A. Yaremchenko, G. C. Mather, A. L. Shaula, I. A. Leonidov, V. L. Kozhevnikov and J. R. Frade, *Solid State Sci.*, 2005, **7**, 355-365.
12. B. Pierozynski, *Int. J. Electrochem. Sci.*, 2011, **6**, 63-77.
13. W. Sheng, H. A. Gasteiger and Y. Shao-Horn, *J. Electrochem. Soc.*, 2010, **157**, B1529-B1536.
14. M. Roos, D. Boecking, K. O. Gyimah, G. Kucerova, J. Bansmann, J. Biskupek, U. Kaiser, N. Huesing and R. J. Behm, *Beilstein J. Nanotechnol.*, 2011, **2**, 593-606.
15. U. A. Paulus, T. J. Schmidt, H. A. Gasteiger and R. J. Behm, *J. Electroanal. Chem.*, 2001, **495**, 134-145.
16. W. C. Chueh, Y. Hao, W. Jung and S. M. Haile, *Nat. Mater.*, 2012, **11**, 155-161.
17. M. Yamaguchi, T. Takamoto and K. Araki, *Sol. Energy Mater. Sol. Cells*, 2006, **90**, 3068-3077.
18. A. Itou, T. Asano, D. Inoue, H. Arase, A. Matsushita, N. Hayashi, R. Futakuchi, K. Inoue, M. Yamamoto, E. Fujii, T. Nakagawa, Y. Anda, H. Ishida, T. Ueda, O. Fidaner, M. Wiemer and D. Ueda, *Jpn. J. Appl. Phys.*, 2014, **53**, 1-5.
19. J. Yoon, A. J. Baca, S. I. Park, P. Elvikis, J. B. Geddes, L. F. Li, R. H. Kim, J. L. Xiao, S. D. Wang, T. H. Kim, M. J. Motala, B. Y. Ahn, E. B. Duoss, J. A. Lewis, R. G. Nuzzo, P. M. Ferreira, Y. G. Huang, A. Rockett and J. A. Rogers, *Nat. Mater.*, 2008, **7**, 907-915.

20. F. Meinardi, A. Colombo, K. A. Velizhanin, R. Simonutti, M. Lorenzon, L. Beverina, R. Viswanatha, V. I. Klimov and S. Brovelli, *Nat. Photonics*, 2014, **8**, 392-399.
21. E. Borgarello, J. Kiwi, E. Pelizzetti, M. Visca and M. Gratzel, *J. Am. Chem. Soc.*, 1981, **103**, 6324-6329.
22. J. Kiwi, *J. Phys. Chem.* , 1985, **89**, 2437-2439.
23. P. Gomathisankar, D. Yamamoto, H. Katsumata, T. Suzuki and S. Kaneco, *Int. J. Hydrogen Energy*, 2013, **38**, 5517-5524.
24. J. R. Smith, T. H. Van Steenkiste and X. G. Wang, *Phys. Rev. B*, 2009, **79**, 4.
25. Y. K. Chen, C. X. Xiang, S. Hu and N. S. Lewis, *J. Electrochem. Soc.*, 2014, **161**, F1101-F1110.
26. B. Parkinson, *Sol. Cells*, 1982, **6**, 177-189.
27. S. Licht, *Adv. Mater.*, 2011, **23**, 5592-5612.
28. P. V. Kamat, M. D. Karkhanavala and P. N. Moorthy, *J. Appl. Phys.*, 1979, **50**, 4228-4230.
29. K. Rajeshwar, P. Singh and R. Thapar, *J. Electrochem. Soc.*, 1981, **128**, 1750-1754.
30. C. D. Lokhande and S. H. Pawar, *Sol. Energy Mater.*, 1982, **7**, 313-318.
31. J. F. McCann, M. Skyllas-Kazacos and D. Haneman, *Nature*, 1981, **289**, 780-782.
32. P. S. Patil, C. D. Lokhande and S. H. Pawar, *J. Phys. D: Appl. Phys.*, 1989, **22**, 550-554.
33. D. K. Bora, A. Braun and E. C. Constable, *Energy Environ. Sci.*, 2013, **6**, 407-425.
34. K. Sivula, F. Le Formal and M. Gratzel, *ChemSusChem*, 2011, **4**, 432-449.
35. F. J. Morin, *Phys. Rev.*, 1954, **93**, 1195-1199.
36. A. G. Joly, J. R. Williams, S. A. Chambers, G. Xiong, W. P. Hess and D. M. Laman, *J. Appl. Phys.*, 2006, **99**, 6.
37. S. R. Pendlebury, M. Barroso, A. J. Cowan, K. Sivula, J. W. Tang, M. Gratzel, D. Klug and J. R. Durrant, *Chem. Commun.*, 2011, **47**, 716-718.
38. M. P. Dareedwards, J. B. Goodenough, A. Hamnett and P. R. Trevellick, *J. Chem. Soc., Faraday Trans. 1*, 1983, **79**, 2027-2041.
39. K. Sivula, *J. Phys. Chem. Lett.*, 2013, **4**, 1624-1633.
40. F. K. Meng, J. T. Li, S. K. Cushing, J. Bright, M. J. Zhi, J. D. Rowley, Z. L. Hong, A. Manivannan, A. D. Bristow and N. Q. Wu, *ACS Catal.*, 2013, **3**, 746-751.
41. K. Sivula, R. Zboril, F. Le Formal, R. Robert, A. Weidenkaff, J. Tucek, J. Frydrych and M. Gratzel, *J. Am. Chem. Soc.*, 2010, **132**, 7436-7444.
42. S. D. Tilley, M. Cornuz, K. Sivula and M. Gratzel, *Angew. Chem., Int. Ed.*, 2010, **49**, 6405-6408.
43. H. Dotan, O. Kfir, E. Sharlin, O. Blank, M. Gross, I. Dumchin, G. Ankonina and A. Rothschild, *Nat. Mater.*, 2012, **12**, 158-164.
44. F. Le Formal, M. Gratzel and K. Sivula, *Adv. Funct. Mater.*, 2010, **20**, 1099-1107.
45. D. K. Zhong and D. R. Gamelin, *J. Am. Chem. Soc.*, 2010, **132**, 4202-4207.
46. C. Du, X. G. Yang, M. T. Mayer, H. Hoyt, J. Xie, G. McMahon, G. Bischoping and D. W. Wang, *Angew. Chem., Int. Ed.*, 2013, **52**, 12692-12695.
47. F. Le Formal, N. Tetreault, M. Cornuz, T. Moehl, M. Gratzel and K. Sivula, *Chem. Sci.*, 2011, **2**, 737-743.
48. T. Hisatomi, F. Le Formal, M. Cornuz, J. Brillet, N. Tetreault, K. Sivula and M. Gratzel, *Energy Environ. Sci.*, 2011, **4**, 2512-2515.
49. L. Steier, I. Herraiz-Cardona, S. Gimenez, F. Fabregat-Santiago, J. Bisquert, S. D. Tilley and M. Grätzel, *Adv. Funct. Mater.*, 2014, **24**, 7681-7688.
50. R. F. G. Gardner, R. L. Moss and D. W. Tanner, *Br. J. Appl. Phys.*, 1966, **17**, 55.
51. D. W. Tanner, F. Sweett and R. F. G. Gardner, *Br. J. Appl. Phys.*, 1964, **15**, 1041-1043.
52. B. M. Warnes, F. F. Aplan and G. Simkovich, *Solid State Ionics*, 1984, **12**, 271-276.
53. B. Zhao, T. C. Kaspar, T. C. Droubay, J. McCloy, M. E. Bowden, V. Shutthanandan, S. M. Heald and S. A. Chambers, *Phys. Rev. B*, 2011, **84**.
54. A. J. Cowan, C. J. Barnett, S. R. Pendlebury, M. Barroso, K. Sivula, M. Gratzel, J. R. Durrant and D. R. Klug, *J. Am. Chem. Soc.*, 2011, **133**, 10134-10140.

55. B. Klahr, S. Gimenez, F. Fabregat-Santiago, T. Hamann and J. Bisquert, *J. Am. Chem. Soc.*, 2012, **134**, 4294-4302.
56. H. L. Wang, T. Deutsch and J. A. Turner, *J. Electrochem. Soc.*, 2008, **155**, F91-F96.
57. F. D. Lin and S. W. Boettcher, *Nat. Mater.*, 2014, **13**, 81-86.
58. T. Lindgren, H. L. Wang, N. Beermann, L. Vayssieres, A. Hagfeldt and S. E. Lindquist, *Sol. Energy Mater. Sol. Cells*, 2002, **71**, 231-243.
59. P. Wurfel, *Physics of Solar Cells: From Principles to New Concepts*, WILEY-VCH: Weinheim, 2005.
60. H. A. Zondag, *Renewable Sustainable Energy Rev.*, 2008, **12**, 891-959.
61. P. Singh and N. M. Ravindra, *Sol. Energy Mater. Sol. Cells*, 2012, **101**, 36-45.
62. B. M. Klahr, A. B. F. Martinson and T. W. Hamann, *Langmuir*, 2011, **27**, 461-468.
63. B. M. Klahr and T. W. Hamann, *J. Phys. Chem. C*, 2011, **115**, 8393-8399.
64. D. K. Nordstrom, *Geochim. Cosmochim. Acta*, 1977, **41**, 1835-1841.
65. M. Turcu, O. Pakma and U. Rau, *Appl. Phys. Lett.*, 2002, **80**, 2598-2600.
66. D. L. Pulfrey, *IEEE Trans. Electron Devices*, 1978, **25**, 1308-1317.
67. A. Royne, C. J. Dey and D. R. Mills, *Sol. Energy Mater. Sol. Cells*, 2005, **86**, 451-483.